



**HAL**  
open science

# Hydrogeophysical characterization and determination of petrophysical parameters by integrating geophysical and hydrogeological data at the limestone vadose zone of the Beauce aquifer

Mohamad Abbas, Jacques Deparis, Arnaud Isch, Céline Mallet, Clara Jodry,  
Mohamed Azaroual, Bouamama Abbar, Jean-Michel Baltassat

## ► To cite this version:

Mohamad Abbas, Jacques Deparis, Arnaud Isch, Céline Mallet, Clara Jodry, et al.. Hydrogeophysical characterization and determination of petrophysical parameters by integrating geophysical and hydrogeological data at the limestone vadose zone of the Beauce aquifer. *Journal of Hydrology*, 2022, pp.128725. 10.1016/j.jhydrol.2022.128725 . hal-03864896

**HAL Id: hal-03864896**

**<https://brgm.hal.science/hal-03864896v1>**

Submitted on 22 Nov 2022

**HAL** is a multi-disciplinary open access archive for the deposit and dissemination of scientific research documents, whether they are published or not. The documents may come from teaching and research institutions in France or abroad, or from public or private research centers.

L'archive ouverte pluridisciplinaire **HAL**, est destinée au dépôt et à la diffusion de documents scientifiques de niveau recherche, publiés ou non, émanant des établissements d'enseignement et de recherche français ou étrangers, des laboratoires publics ou privés.

# Journal Pre-proofs

## Research papers

Hydrogeophysical characterization and determination of petrophysical parameters by integrating geophysical and hydrogeological data at the limestone vadose zone of the Beauce aquifer

M. Abbas, J. Deparis, A. Isch, C. Mallet, C. Jodry, M. Azaroual, B. Abbar, J.M. Baltassat

PII: S0022-1694(22)01295-1  
DOI: <https://doi.org/10.1016/j.jhydrol.2022.128725>  
Reference: HYDROL 128725

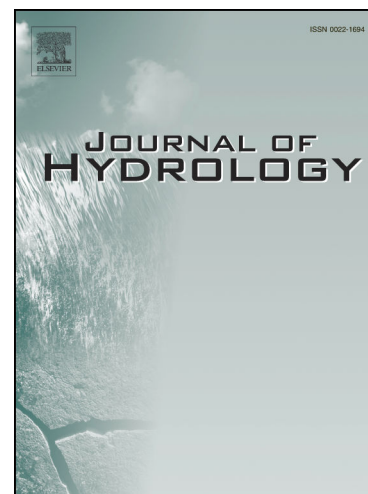
To appear in: *Journal of Hydrology*

Received Date: 15 February 2022  
Revised Date: 10 October 2022  
Accepted Date: 11 October 2022

Please cite this article as: Abbas, M., Deparis, J., Isch, A., Mallet, C., Jodry, C., Azaroual, M., Abbar, B., Baltassat, J.M., Hydrogeophysical characterization and determination of petrophysical parameters by integrating geophysical and hydrogeological data at the limestone vadose zone of the Beauce aquifer, *Journal of Hydrology* (2022), doi: <https://doi.org/10.1016/j.jhydrol.2022.128725>

This is a PDF file of an article that has undergone enhancements after acceptance, such as the addition of a cover page and metadata, and formatting for readability, but it is not yet the definitive version of record. This version will undergo additional copyediting, typesetting and review before it is published in its final form, but we are providing this version to give early visibility of the article. Please note that, during the production process, errors may be discovered which could affect the content, and all legal disclaimers that apply to the journal pertain.

© 2022 Published by Elsevier B.V.



1 **Hydrogeophysical characterization and determination of petrophysical parameters by integrating**  
2 **geophysical and hydrogeological data at the limestone vadose zone of the Beauce aquifer**

3 M. Abbas<sup>1</sup> \*, J. Deparis<sup>2</sup>, A. Isch<sup>1</sup>, C. Mallet<sup>1</sup>, C. Jodry<sup>3</sup>, M. Azaroual<sup>1,2</sup>, B. Abbar<sup>1</sup>, and J. M.  
4 Baltassat<sup>2</sup>

5 <sup>1</sup> Univ. Orléans, CNRS, BRGM, ISTO, UMR 7327, F-45071, Orléans, France.

6 <sup>2</sup> BRGM, French Geological Survey, 45060 Orléans, France.

7 <sup>3</sup> UNISTRA, Azerbaijan State Oil and Industry University, French Azerbaijani University,  
8 Baku, Azerbaijan.

9

10 \*Corresponding Author ([abbas\\_mohammad@live.com](mailto:abbas_mohammad@live.com))

11

12

13

14

15

16

17

18

19

20

21

22

23

24

25

26

27

28

29

30

**31 Abstract**

32 The hydrological characterization of the vadose zone remains a major challenge considering  
33 the spatiotemporal variability of its properties and the limitations associated with hydrological  
34 measurements techniques. Geophysical methods, in particular the DC-resistivity and ground  
35 penetrating radar, can provide large scale images of hydrogeological structures and a non-  
36 invasive assessment of the subsurface dynamic processes. However, these approaches rely on  
37 the accuracy of the petrophysical relationships connecting the geophysical parameters to  
38 hydrogeological ones, where the site-specific determination of the associated petrophysical  
39 parameters is considered crucial. The first objective of this study was to investigate the  
40 relationship between the water content, geological properties, and geophysical attributes at the  
41 vadose zone of a vulnerable limestone aquifer. The second objective aimed to obtain the  
42 Archie's and Complex Refractive Index Model (CRIM) petrophysical parameters by using  
43 borehole electrical resistivity and cross-hole ground penetrating radar data. For this purpose,  
44 we adopted a grid search inversion algorithm where the field geophysical data were integrated  
45 with water content profiles simulated by using HYDRUS-1D. The vadose zone profile was  
46 divided into three layers, and the inversion was carried out for the petrophysical parameters in  
47 each of the model layers. The electrical resistivity and relative dielectric permittivity data  
48 showed a very good correspondence with the simulated and experimental water content  
49 distributions along the vadose zone profile. The petrophysical parameters estimated by the  
50 inversion showed values that fall in the ranges reported in the literature. Similar values have  
51 been observed in the different model layers, with slight differences that were attributed to the  
52 vertical heterogeneities associated with the alteration and fracturation features of the limestone  
53 vadose zone. This study showed a very good correlation between geophysical, hydrogeological  
54 and geological data, and highlighted the presence of heterogeneities that can have profound  
55 effects on the vadose zone water dynamics.

56 **Key Words:** Electrical Resistivity, Ground Penetrating Radar, Archie, Complex Refractive  
57 Index Model, Water Content.

## 58 **1. Introduction**

59 Improved understanding of water flow and transport processes in the vadose zone (VZ) is  
60 crucial, considering the critical role this compartment of the subsurface plays within the  
61 biosphere and in the transmission of water and contaminants from the surface to the  
62 groundwater. Contamination sources mainly originate in the VZ where the transfer of  
63 contaminants is impacted by the medium heterogeneities (e.g., fractures, induced preferential  
64 flow and rapid infiltration), and by interactions involving a complex interplay between coupled  
65 physical, geochemical, and microbial processes (Arora et al., 2019; Stephens, 2019; Nimmo,  
66 2005). Therefore, a better knowledge of the hydrogeological processes and water content  
67 distribution within the VZ is essential to protect groundwater resources.

68 Conventionally, water content measurements were carried out by single-point techniques, such  
69 as time domain reflectometry (TDR) or neutron probes (He et al., 2021; Isch et al., 2019;  
70 Skierucha et al., 2012; Evett, 2008; Verhoef et al., 2006; Evett, 2003). Advancements in these  
71 techniques (e.g., multi-TDR systems) provided the possibility of time-lapse water content  
72 monitoring and eventual preferential flow paths detection (Herkelrath et al., 1991). However,  
73 such measurements are intrusive, limited to very shallow depths, and provide restricted  
74 information at only a series of point locations. These measurements are often not representative  
75 of the field scale spatial water content distribution (Robinson et al., 2003). The difficulties  
76 involved in obtaining 2-D or 3-D hydrologic images by exploiting such sparse local data  
77 introduced geophysical methods as alternative ways of monitoring water content distribution  
78 and water fluxes within the VZ (Binley et al., 2015; Vereecken et al., 2006; Rubin and Hubbard,  
79 2005).

80 Geophysical methods have shown a great potential in providing large-scale and high spatial  
81 resolution images of the subsurface hydrogeological processes (Binley et al., 2015; 2010).  
82 Several surface and cross-borehole geophysical methods have been recently used for different  
83 hydrological applications. These methods include the ground penetrating radar (GPR) (Dafflon  
84 et al., 2011; Lunt et al., 2005; Binley et al., 2001), seismic techniques (Blazevic et al., 2020),  
85 electrical resistivity (ER) (Mallet et al., 2021; Johnson et al., 2015; Robinson et al., 2008), self-  
86 potential (Abbas et al, 2017; Ahmed et al., 2014; Jardani et al., 2012), induced polarization  
87 (Johnson et al., 2010) and nuclear magnetic resonance (Vilhelmsen et al., 2014). Additionally,  
88 geophysical methods have been recently used to characterize and quantify processes and  
89 interactions in the soil–rhizosphere–atmosphere agricultural ecosystem continuum (Garré et al.,  
90 2021).

91 In particular, the GPR and ER methods have been frequently used to investigate water flow  
92 dynamics and identify hydrodynamic parameters (Klotzsche et al., 2019, 2018; Paz et al., 2017;  
93 Binley et al., 2015). Thanks to well-established petrophysical relationships between water  
94 content and both electrical resistivity (e.g., Archie, 1942) and dielectric permittivity (e.g., Topp  
95 et al., 1980) of porous media, these methods can provide valuable information on water flow  
96 that can be used to parameterize and constrain hydrogeological models. Relative variations of  
97 water content distribution in VZ profiles have been successfully estimated by GPR and ER data.  
98 These observations were used to monitor infiltration experiments and visualize flow patterns,  
99 quantify petrophysical parameters, characterize preferential flow pathways in fractured media  
100 (De Jong et al., 2020; Gance et al., 2016; Wehrer and Slater, 2015; Klotzsche et al., 2013;  
101 Steelman and Endres, 2011; Brunet et al., 2010; Cassiani et al., 2009b ; Looms et al., 2008;  
102 Linde et al., 2006; Kowalsky et al., 2005; Huisman et al., 2003; Binley et al., 2002a; Hubbard  
103 et al., 2001a), and even assess the variations of the soil water content associated with root water  
104 uptake (Mary et al., 2018; Hagrey, 2007).

105 Generally, the water content estimates derived from GPR and ER data showed high accuracy  
106 and a good reproducibility. However, geophysical methods cannot directly provide water  
107 content values. This approach is dependent on the empirical relationships between the sensed  
108 physical parameters and the subsurface parameters of interest (e.g., porosity and water  
109 saturation), especially in complex heterogeneous mediums such as carbonate environments,  
110 which are often characterized by a complex multiple-porosity system consisting of matrix  
111 porosity and fissures, vugs, fractures and karst networks (Mallet et al., 2022; Aldana et al.,  
112 2021; Ammar and Kamal, 2017; Mount and Comas, 2014 ; Lucia, 2007). Difficulties arise in  
113 the need of time-consuming and expensive laboratory calibration of the petrophysical  
114 relationships that are basically suitable only for homogeneous formations, and influenced by  
115 properties such as the porosity and tortuosity patterns of the medium under study (Mohamed  
116 and Hamada, 2017; Glover, 2016). Estimating parameters such as the water content and  
117 porosity from geophysical data by using documented literature values of petrophysical  
118 parameters can induce a lot of uncertainties in the absence of site-specific calibration.  
119 Achieving an efficient determination of site-specific petrophysical parameters is expected to  
120 reduce such uncertainties, and can provide a large-scale and time-saving estimation of water  
121 content by avoiding destructive and time-consuming hydrogeological measurements and  
122 laboratory calibrations.

123 The presented study is carried out within the framework of the “Observatory of Transfers in the  
124 Vadose Zone” (O-ZNS) platform. The general objective of the O-ZNS platform is to investigate  
125 the water-rock-biosphere interactions and their associated mass and heat transfer processes in  
126 the VZ. This can provide a better understanding of the VZ dynamics and coupled processes by  
127 providing physical, biogeochemical and spatially resolved hydrodynamic parameters capable  
128 of characterizing water flow patterns and parameterizing transport models. This study first  
129 investigates the relationship between geophysical attributes, water content and geological

130 heterogeneities at the vadose zone of a vulnerable limestone aquifer. An inversion algorithm is  
131 then used to obtain the Archie's and CRIM's petrophysical parameters by integrating borehole  
132 electrical resistivity and cross-hole ground penetrating radar data with water content profiles  
133 simulated by HYDRUS-1D.

## 134 **2. Study site**

### 135 **2.1. Description**

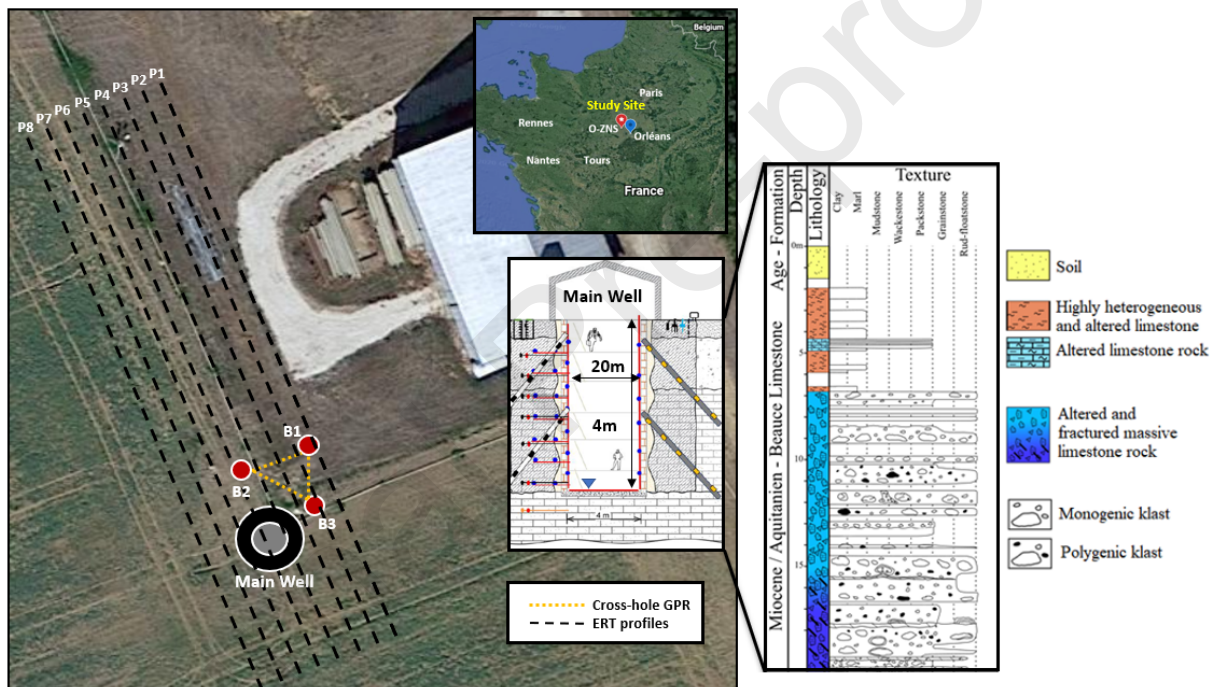
136 This study was carried out at the O-ZNS observatory, located in the vicinity of the Beauce  
137 limestone aquifer at an agricultural site in Villamblain, France (Fig. 1) (DMS coordinates: X =  
138  $48^{\circ}1'5.131''$ ; Y =  $1^{\circ}34'55.333''$ ). The observatory offers a unique experimental setup, composed  
139 of an exceptional well having a depth of 20 m and a diameter of 4 m, along with a number of  
140 instrumented boreholes and piezometers. Additionally, the observatory will be equipped with  
141 innovative complementary environmental sensors such as fiber-optic sensors (e.g., distributed  
142 acoustic sensing, distributed temperature sensing), water content monitoring probes (e.g.,  
143 TDR), and samplers. These sensors can provide quantitative measurements relative to fluid and  
144 heat transfer processes within the VZ. During its exploitation, which is planned for several  
145 decades, the observatory will allow acquiring original and unique data on the mass (water,  
146 solutes, organic and inorganic contaminants, gases, etc.) and heat (induced by temperature  
147 gradients, microbiological reactions, etc.) transfer processes across the continuum "Soil-VZ-  
148 Capillary Fringe -Aquifer" for environmental issues and water management. A detailed  
149 description of the observatory instrumentation setup can be found in Abbar et al. (2021).

### 150 **2.2. Geology**

151 Direct observations of undisturbed cores complemented with optical log imagery revealed  
152 significant vertical and lateral lithological heterogeneities within the VZ units. Three main  
153 lithological units have been identified by the direct core observations (Fig. 1): (1) A first top



154 soil unit having a thickness ranging between 0.9 and 1.8 m, and a silt loam texture referred to  
 155 as a Hypereutric Cambisol (IUSS Working Group WRB, 2015); (2) a second unit characterized  
 156 by highly heterogeneous and altered (i.e., fractures, weathering, oxidation) incoherent  
 157 limestone facies reaching a depth of around 7 m; and (3) a third unit of hard limestone rock  
 158 (Pithiviers limestone) extending from a depth of around 7 m down to 20 m with a clear evolution  
 159 of alteration, fracturation and karstification with depth. The water table had an average depth  
 160 ranging between 16.5 m and 20.5 m over the last decade, with observed historical variations  
 161 ranging between 14.5 m and 22.5 m since 1966 (Isch et al., 2022).



162  
 163 **Fig. 1.** Study site location, instrumentation, geology and geophysical measurements setup. The  
 164 figure only shows the boreholes used for this study, several other boreholes surrounding the  
 165 main well are present at the study site.

### 166 3. Methods

#### 167 3.1. Geophysical data acquisition

168 The O-ZNS infrastructure allows the combination of different geophysical methods and focuses  
169 on integrating borehole, cross-hole and surface geophysical techniques that are sensitive to  
170 transfer and flow processes. In this section, we present the acquisition protocols of the electrical  
171 resistivity tomography (ERT), borehole ER and cross-hole GPR data used in this study.

### 172 **3.1.1. Electrical Resistivity**

173 A total of 8 ERT profiles were acquired on the 18<sup>th</sup> of April, 2019 by using a Syscal-Pro 96  
174 resistivity meter (Iris Instruments, France) connected to a Syscal Switch Pro 96. The profiles  
175 had 48 electrodes each, with an inter-profile spacing of 5 m (Fig. 1). A 2.5 m electrodes spacing  
176 was chosen in order to ensure both, an acceptable resolution, and a maximum investigation  
177 depth of about 23 m. The measurements were acquired in Dipole-Dipole and Wenner-  
178 Schlumberger configurations. Basic filtering steps have been conducted on the acquired ERT  
179 profiles (e.g., exterminating bad data points). The profiles were then inverted by Res2Dinv  
180 (Loke and Barker,1996) that uses a smoothness-constrained Gauss-Newton least-squares  
181 inversion technique to obtain a 2D electrical resistivity model of the subsurface from the field  
182 apparent resistivity data (Griffiths and Barker, 1993). The result is a 2D smoothness-constrained  
183 distribution of electrical resistivity in the VZ. The effect of temperature variations was  
184 considered negligible on the electrical resistivity data along the first 20 meters of the subsurface.  
185 This was assumed due to the observed low variations of temperature as a function of depth in  
186 the VZ at this time of the year.

187 On the other hand, the ER borehole data were obtained from three different boreholes logs (B1,  
188 B2 and B3, cf. Fig. 1) on the 23<sup>rd</sup> of March, 2017 by means of the dual induction-laterolog  
189 (DIL) method. This method consists of focused electrical measurements that rely on transmitter  
190 and receiver coils. The measurements are based on an alternating current that generate eddy  
191 currents which in turn produce a secondary electromagnetic field. The latter induces an  
192 alternating voltage proportional to the formation electrical conductivity in the receiver coil. The

193 transmitter-receiver pair which uses a low frequency is designed to minimize the effects of the  
 194 borehole and optimize the depth of investigation and the measurement vertical resolution. A  
 195 measurement point spacing of 2 cm was used, with a maximum penetration depth varying  
 196 between 18 m and 19 m depending on each of the borehole's maximum accessible depth.

### 197 **3.1.2. Ground Penetrating Radar**

198 The cross-hole GPR measurements were acquired by using a ProEx GPR system (Malå  
 199 Geosciences) on the 24<sup>th</sup> of January, 2019. The measurements were done by using 100 MHz  
 200 borehole antennae with a sampling frequency of 1000 MHz and a measurement period of  
 201 240 ns. Zero offset profiles (ZOP) were acquired between the three boreholes B1, B2 and B3  
 202 (TXB2\_RXB1, TXB1\_RXB3 and TXB2\_RXB3) (Fig. 1). The ZOP method is a commonly  
 203 used approach for borehole GPR acquisition surveys (Klotzsche et al., 2019). Throughout the  
 204 ZOP measurements, the transmitting (Tx) and receiving (Rx) antennas are moved  
 205 simultaneously in two different boreholes with a fixed step size. To conduct the ZOP  
 206 measurements, the antenna were first pushed to the bottom of each of the boreholes where the  
 207 maximum accessible depth was 18.98 m (water table). The antennae were then pulled  
 208 simultaneously towards the surface by using a 0.5 m fixed step size.

209 One-dimensional velocity profiles were then determined by a standard ray-based analysis  
 210 approach. For simplicity, the medium was assumed to have no horizontal variation of velocity  
 211 while obtaining the one-dimensional velocity profiles. After picking the first arrivals (in  
 212 ReflexW©), the arrival time ( $t$ ) and the distance between the boreholes were used to determine  
 213 the GPR electromagnetic wave velocity ( $v$ ) through the following equation:

$$v = \left( \frac{d}{t - T_0} \right), \quad (1)$$

214 where  $T_0$  is the time-zero offset, which was obtained by conducting multi-offset measurements  
 215 with the antenna in free-space. In low-loss and non-magnetic material such as carbonate

216 formations (e.g., limestone), the relative dielectric permittivity ( $\epsilon_r$ ) can be then determined at  
217 different depths by using the following equation:

$$\epsilon_r = (c/v)^2, \quad (2)$$

218 where  $c$  is the velocity of an electromagnetic wave in vacuum ( $\sim 0.3$  m/ns). Relative dielectric  
219 permittivity profiles were then determined from the obtained velocity profiles by using Eq. 2.

## 220 **3.2. Hydraulic properties measurements and simulation of water flow within the VZ**

### 221 **3.2.1. Hydraulic properties of the vadose zone samples**

222 Fifteen undisturbed samples representative of the VZ (0-20 m deep) were chosen according to  
223 the lithological observations made from the three cored boreholes B1, B2 and B3 (Isch et al.,  
224 2022). The samples included three soil samples ( $S_A$ ,  $S_B$  and  $S_C$ ), four soft sediments and  
225 powdery limestone samples ( $P_A$ ,  $P_B$ ,  $P_C$  and  $P_D$ ), two calcareous sand samples ( $I_A$  and  $I_B$ ), and  
226 six limestone rock samples ( $R_A$ ,  $R_B$ ,  $R_C$ ,  $R_D$ ,  $R_E$  and  $R_F$ ). These samples were used to estimate  
227 the water retention  $\theta(h)$  and hydraulic conductivity  $K(h)$  curves by applying the multistep  
228 outflow method (Aldana et al., 2021). The multistep outflow experiments were conducted by  
229 using a triaxial system based on the experimental procedure described by Eching et al. (1994).  
230 The hydraulic conductivity was calculated from the outflow data based on the method described  
231 by Gardner (1956).

### 232 **3.2.2. Simulation of water flow in the vadose zone**

233 Simulation of water flow within the VZ was then performed over a 55 years period (1966-2020)  
234 on a 23 m deep VZ profile (borehole B2) composed of fifteen layers and reconstituted with the  
235 HYDRUS-1D software (Šimůnek et al., 2016). The simulation of water flow was based on the  
236 one-dimensional vertical water flow in the VZ described by Richards equation (Richards,  
237 1931):

$$\frac{\partial \theta}{\partial t} = \frac{\partial}{\partial z} \left[ K \left( \frac{\partial h}{\partial z} + 1 \right) \right] - S, \quad (3)$$

238 where  $\theta$  is the volumetric water content ( $\text{cm}^3/\text{cm}^3$ ),  $z$  is the coordinate along the vertical axis  
 239 (cm),  $t$  is the time,  $h$  is the matric head (cm),  $K$  is the hydraulic conductivity (cm/d) and  $S$  is a  
 240 sink-source term. The Mualem-Van Genuchten analytical model (MVG) was used for the  
 241 description of the VZ hydraulic properties. The van Genuchten's expression (van Genuchten,  
 242 1980) was used to describe the water retention curve:

$$\theta(h) = \begin{cases} \theta_r + \frac{\theta_s - \theta_r}{[1 + |\alpha h|^n]^m} & h < 0 \\ \theta_s & h \geq 0 \end{cases} \quad (4)$$

$$\text{with} \quad m = 1 - \frac{1}{n} \quad n > 1,$$

243 where  $\theta_r$  and  $\theta_s$  are the residual and saturated volumetric water content ( $\text{cm}^3/\text{cm}^3$ ) respectively.  
 244  $\alpha$  is an empirical parameter related to the matric head ( $\text{cm}^{-1}$ ), and  $n$  is a pore size distribution  
 245 parameter (-). The statistical pore connection model of Mualem (1976) was then used to predict  
 246 the hydraulic conductivity from the water retention curve:

$$K(h) = K_s S_e^l \left[ 1 - \left( 1 - S_e^{\frac{1}{m}} \right)^m \right]^2 \quad (5)$$

$$\text{with} \quad S_e = \frac{\theta - \theta_r}{\theta_s - \theta_r},$$

247 where  $K_s$  is the saturated hydraulic conductivity (cm/d),  $S_e$  is the effective saturation (-) and  $l$   
 248 is a pore connectivity parameter (-) fixed at the value of 0.5 (Mualem, 1976). The measured  
 249 water retention and hydraulic conductivity data were fitted to the  $\theta(h)$  and  $K(h)$  curves with the  
 250 MVG model (Eq. 4 and Eq. 5) by using the RETC software (van Genuchten et al., 1991) to  
 251 infer the VZ hydraulic properties used in our simulations. The representation of the VZ profile

252 for B2, the values of experimental and fitted (with RETC) saturated volumetric water content  
 253 ( $\theta_s$ ) and fitted hydraulic conductivity ( $K_s$ , in cm/d) are given in Table 1. Water table level and  
 254 meteorological data were collected from monitoring stations located at the villages of Poiseaux  
 255 (4 km from the study site) and Bricy (20 km from the study site) respectively. While the weather  
 256 conditions at the study site may differ slightly during intense and localized rainy events relative  
 257 to those observed at the Bricy station, these are however considered to be representative over a  
 258 period of more than 50 years.

259 **Table 1.** (a) Description of the samples considered for the representation of the VZ profile and  
 260 the simulation of water flow with HYDRUS-1D: depth, description, saturated water content ( $\theta_s$   
 261 ), experimental saturated water content ( $\theta_{sExp.}$ ), hydraulic conductivity ( $K_s$ ),  $\alpha$ , and  $n$ .

Geological Unit	Depth (m)	Sample	Description	$\theta_s$ (cm <sup>3</sup> /cm <sup>3</sup> )	$\theta_{sExp.}$ (cm <sup>3</sup> /cm <sup>3</sup> )	$K_s$ (cm/d)	$\alpha$ cm <sup>-1</sup>	$n$ (/)
1	0.00-0.30	S <sub>A</sub>	Soil	0.4735	0.4864	30.24	0.0242	1.15
	0.31-0.60	S <sub>B</sub>	Soil	0.4661	0.4612	53.57	0.0242	1.16
	0.61-0.90	S <sub>C</sub>	Soil	0.5002	0.4162	47.52	0.0366	1.16
2	0.91-1.30	P <sub>A</sub>	Powdery limestone	0.4511	0.4230	7.31	0.0247	1.17
	1.30-3.50	P <sub>B</sub>	Powdery limestone	0.3659	0.3525	0.455	0.0073	1.25
	3.51-4.10	I <sub>A</sub>	Calcareous sand	0.3918	0.3775	35.22	0.0715	1.20
	4.11-4.60	P <sub>C</sub>	Powdery limestone	0.2969	0.3080	0.143	0.0031	1.22
	4.61-4.90	I <sub>B</sub>	Calcareous sand	0.3698	0.4336	285.49	0.1600	1.23
	4.91-5.20	R <sub>A</sub>	Altered rock	0.2984	0.3400	5000	0.5156	1.36
	5.21-5.50	I <sub>B</sub>	Calcareous sand	0.3698	0.4336	285.49	0.1600	1.23
	5.51-6.60	P <sub>D</sub>	Powdery limestone	0.3527	0.3491	0.185	0.0040	1.22
3	6.61-9.00	R <sub>B</sub>	Massive rock	0.1547	0.1499	1.32	0.0150	1.16
	9.01-11.20	R <sub>D</sub>	Massive rock	0.0949	0.1180	0.402	0.0096	1.17
	11.21-11.40	R <sub>C</sub>	Massive rock	0.0504	0.0491	0.0097	0.0014	1.23
	11.41-14.00	R <sub>D</sub>	Massive rock	0.0949	0.1180	0.402	0.0096	1.17

14.01-16.00	R <sub>E</sub>	Massive rock	0.1172	0.1333	500	0.1266	1.15
16.01-19.00	R <sub>F</sub>	Massive rock	0.1452	0.1639	500	0.1371	1.19

262

## 263 4. Petrophysical Modeling

### 264 4.1. Relative Permittivity

265 The CRIM is a three-phase dielectric mixing model commonly used to describe the relationship  
 266 between relative dielectric permittivity and subsurface properties such as water content and  
 267 porosity (Huisman et., 2003; West et al., 2001; Roth et al., 1990):

$$\varepsilon_r^\alpha = \phi S_w \varepsilon_w^\alpha + (1 - \phi) \varepsilon_s^\alpha + \phi(1 - S_w) \varepsilon_a^\alpha, \quad (6)$$

268 where  $\phi$  and  $S_w$  are the porosity and water saturation respectively,  $\varepsilon_a$  is the relative dielectric  
 269 permittivity of air (given a value of 1),  $\varepsilon_w$  is the relative dielectric permittivity of water,  $\varepsilon_s$  is  
 270 the relative dielectric permittivity of the solid phase, considered as a source of uncertainty to be  
 271 accounted for when using the CRIM.

272 Besides the  $\varepsilon_s$ , the second source of uncertainty to be accounted for is the factor  $\alpha$  which  
 273 describes the orientation of the electrical field with respect to the geological  
 274 formations' geometry (West et al., 2003; Chan and Knight, 1999; Knoll, 1996; Roth et al., 1990;  
 275 Birchak et al., 1974).

### 276 4.2. Electrical Resistivity

277 In geological formations characterized by medium to coarse grained sediments, the grain  
 278 surface conductivity effect can be neglected and the bulk electrical resistivity ( $\rho_0$ ) can be  
 279 related to subsurface properties such as porosity and fluid saturation by the following modified  
 280 form of Archie's equation (Winsauer et al., 1952 ; Archie, 1942):

$$\rho_0 = a\rho_f\phi^{-m}S_w^{-n}, \quad (7)$$

281 where  $\rho_f$  is the fluid or pore water electrical resistivity,  $a$  is an empirical constant originally  
282 referred to as the tortuosity or lithology constant (Winsauer et al., 1952),  $m$  is the cementation  
283 exponent which is considered to be influenced by the degree of cementation of the rock fabric  
284 (Glover, 2010; 2009), and  $n$  is the saturation exponent which is independent of the rock matrix  
285 and describes how the pore water is connected (Glover, 2017; Looms et al., 2008a; Hendrickx  
286 et al., 2002).

287 Even though Archie's law does not take the surface conduction into account, it is considered to  
288 be applicable if the pore fluid conductivity is largely greater than the surface conduction,  
289 especially in the case of low clay content formations such as the limestone rock described within  
290 the VZ of our study site (Fig. 1). The need of including the surface conductivity arises when  
291 other conducting phases such as clay minerals are present in the rock formation. Therefore,  
292 during this study, we applied our approach to the limestone rock facies located at a depth  
293 between 6.61 m and 19 m, where geological and mineralogical studies (Aldana et al., 2021)  
294 suggested that the surface conduction can be practically neglected.

### 295 **4.3. Inversion**

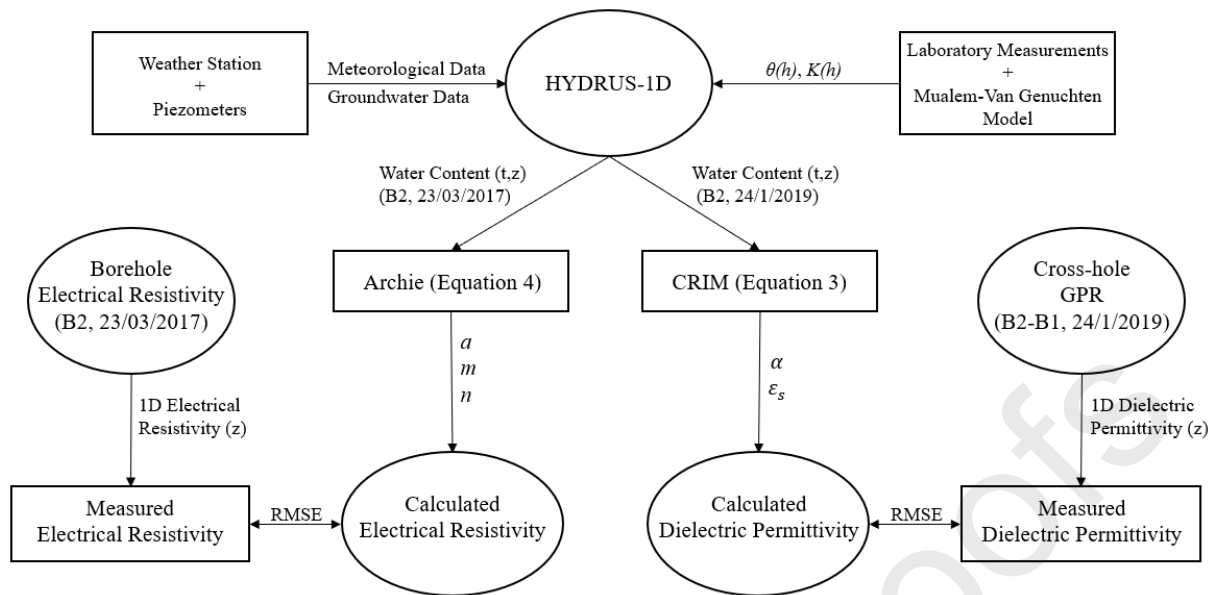
296 This study aims to estimate the Archie's and CRIM's parameters that can vary according to the  
297 study site conditions, and that are considered as sources of uncertainties in the application of  
298 these models for the estimation of water content variations. The numerical approach used in  
299 this study is based on a grid search inversion algorithm (Fig. 2). The inversion workflow is  
300 based on testing the possible combinations of the petrophysical parameters that can provide the  
301 best fit between the measured and simulated data. The estimated data are the electrical  
302 resistivity and relative dielectric permittivity values calculated by using the Archie's and  
303 CRIM's equations respectively. The ER measured data are the 1D electrical resistivity data



304 acquired by the borehole's ER measurements, while the dielectric permittivity measured data  
 305 are those generated from the 1D velocity profiles obtained from the GPR cross-hole  
 306 measurements. The fit between the measured and calculated data is evaluated through  
 307 calculating the corresponding root mean square error (RMSE) while the algorithm varies the  
 308 Archie's (a and m) and CRIM's ( $\alpha$  and  $\epsilon_s$ ) petrophysical parameters to be estimated:

$$\text{RMSE} = \sqrt{\frac{\sum_{i=1}^N (x_i - \hat{x}_i)^2}{N}}, \quad (8)$$

309 where  $x_i$  represents the observed data,  $\hat{x}_i$  represents the data estimated by the model and N is  
 310 the total number of data points. The procedure is done separately for the Archie's and CRIM's  
 311 models. The water content profiles data used to calculate the dielectric permittivity and  
 312 electrical resistivity in the CRIM's and Archie's equation are those simulated by HYDRUS-1D  
 313 software. The geophysical data, water content and porosity data used for both models are  
 314 obtained from the geophysical measurements and hydrogeological model of borehole B2. The  
 315 fluid resistivity in the Archie's equation is given a value of 510  $\mu\text{S}/\text{cm}$  obtained from probes  
 316 and calibrated by laboratory measurements, while the relative dielectric permittivity of water is  
 317 assumed to be 79.5 at a temperature of 22.0 °C (Buchner et al., 1999). The model was divided  
 318 into three layers, and the inversion was carried out for each of the layers separately. This step  
 319 was done to investigate the effect of geological vertical heterogeneities on the obtained  
 320 petrophysical parameters. The model discretization and layering were designed according to  
 321 the geological characteristics and hydrogeological simulations results (see section 5.3.1).



322

323 **Fig. 2.** The inversion algorithm workflow which was done for the Archie and CRIM models  
 324 separately. The inversion procedure is based on finding the combinations of petrophysical  
 325 parameters that can provide the best fit between the measured geophysical data and the  
 326 geophysical profiles calculated by using the water content profiles simulated by HYDRUS-1D.

327 The results analysis is based on obtaining the combined values of the varied Archie ( $a$  and  $m$ )  
 328 and CRIM parameters ( $\alpha$  and  $\epsilon_s$ ) that have the minimal observed RMSE while the algorithm  
 329 fits the calculated and the measured data. The ranges of variability set for each of the parameters  
 330 during the inversion were based on common ranges provided in literature for limestone  
 331 formations. However, the parameters were set to also have values outside these ranges to avoid  
 332 directing the inversion towards literature values, and to compare our results with those reported  
 333 in previous studies. Table 1 shows the ranges of the Archie and CRIM parameters used for this  
 334 inversion and those most commonly reported in the literature for limestone formations. To  
 335 improve the inversion performance and reduce the different parameters dependencies, the  
 336 saturation exponent  $n$  was fixed to a value of 2 and the calculation was done only for the  $a$  and  
 337  $m$  parameters in the Archie equation. Even though values ranging between 1.4 and 2.5 have  
 338 been previously given to  $n$  in the literature for rocks (e.g., Schön, 2004; Sweeney and Jennings,

1960; Rust, 1952), in practice, the saturation exponent is commonly set to 2 for most types of rocks in the absence of laboratory measurements (e.g. Yaramanci et al., 2000; Looms et al., 2008a, 2008b). On the other hand,  $\alpha$  was given a range based on its extreme values which are 1 and -1. The lower boundary (-1) represents the harmonic arrangement of dielectric components in series, while its upper boundary (1) represents the arithmetic arrangement of dielectric components in parallel (Chan and Knight, 2001;1999).

**Table 2** : The ranges of the Archie (a, m and n) and CRIM ( $\alpha$  and  $\epsilon_s$ ) parameters used for the inversion and those commonly reported in the literature for limestone formations.

Model	Parameter	Literature (limestone)	Inversion
Archie	a	$0.2 \leq a \leq 2.3$	$0.1 \leq a \leq 10$
	m	$1.6 \leq m \leq 3$	$1.0 \leq m \leq 10$
	n	$1.5 \leq n \leq 2.5$	n = 2
CRIM	$\alpha$	$-1 \leq \alpha \leq 1$	$-1 \leq \alpha \leq 1$
	$\epsilon_s$	$4 \leq \epsilon_s \leq 11$	$1 \leq \epsilon_s \leq 20$

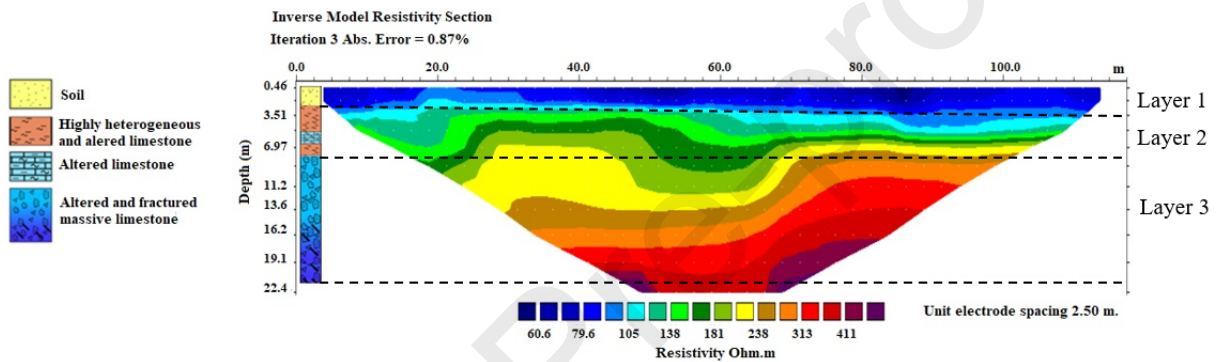
## 5. Results and discussion

### 5.1. Geology

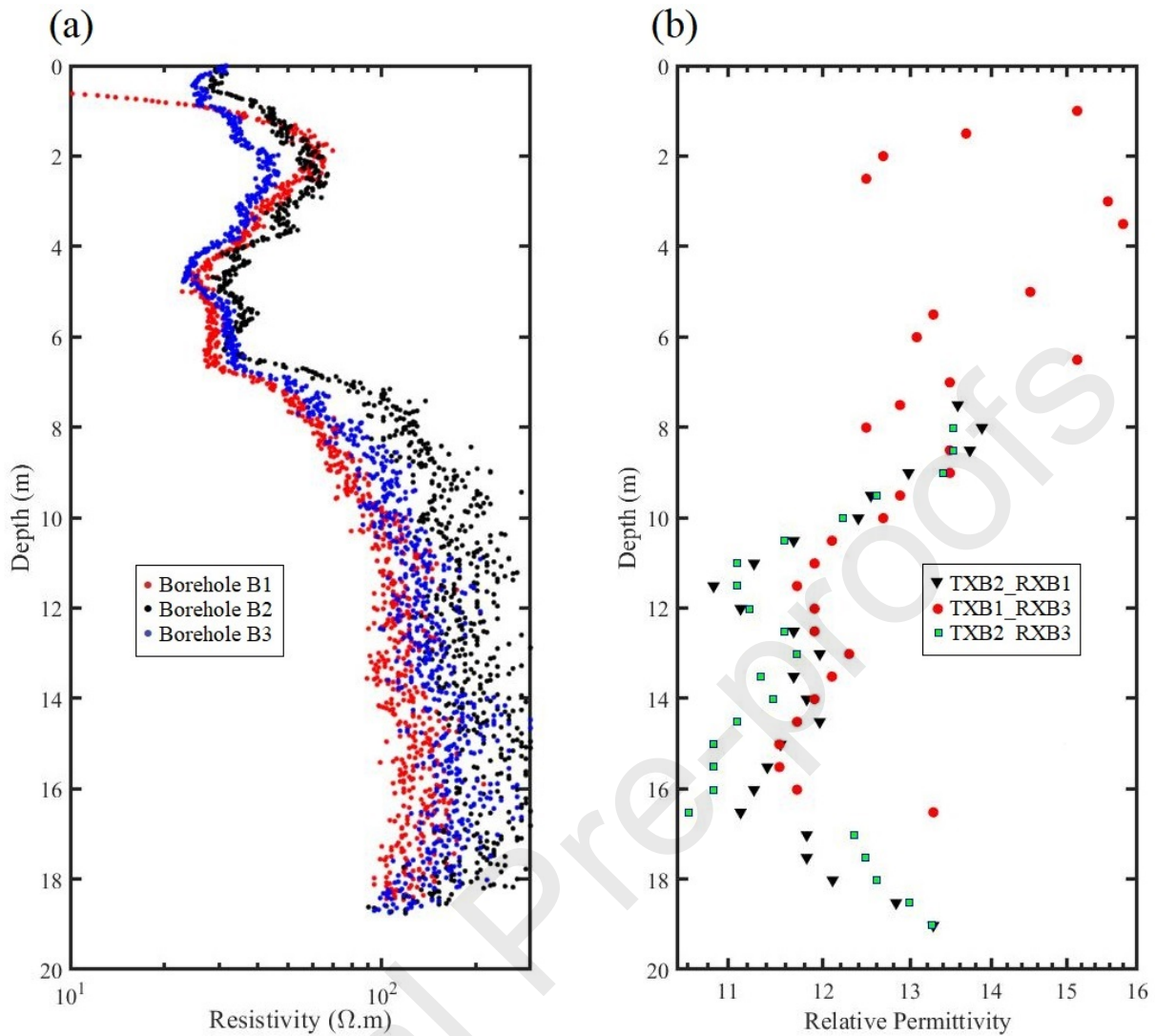
Knowing that a strong coherence was observed between the ERT and borehole ER profiles, throughout this work, the ERT profiles are only used for the lithological description and 2-D representation, while the borehole ER data will be used for the water content analysis and as an input in the inversion for its higher resolution (2 cm) and larger number of data points.

In correspondence with the geological description, the ERT (profile P2 in Fig. 1) showed three main layers corresponding to the three main geological units shown in Fig. 1 (Fig. 3). The data showed a first low ER unit representing the top soil layer. The latter is followed by a moderate

356 ER layer down to a depth of around 7 m. This layer corresponds to the incoherent and altered  
 357 limestone formation. Lateral ER variations (Fig. 3) and dispersed dielectric permittivity values  
 358 (Fig. 4b) were observed in this layer, which reflects the heterogeneity of this formation. A clear  
 359 transition zone between the incoherent limestone layer and the underlying hard limestone rock  
 360 layer is evident in the relative permittivity and ER data at depths between 6.5 m and 9 m. This  
 361 is followed by a third relatively higher ER layer corresponding to the massive limestone rock  
 362 layer. This layer shows lower dielectric permittivity values which started to increase again as  
 363 the measurements got closer to the water table level (Fig. 4b).



364  
 365 **Fig. 3.** The 2D smoothness-constrained distribution of electrical resistivity of profile P2.  
 366 showing 3 main units in accordance with the geology data presented in Fig. 1. All the ERT  
 367 profiles showed similar results in terms of the lithological structure, therefore, only profile P2  
 368 is presented in this work.

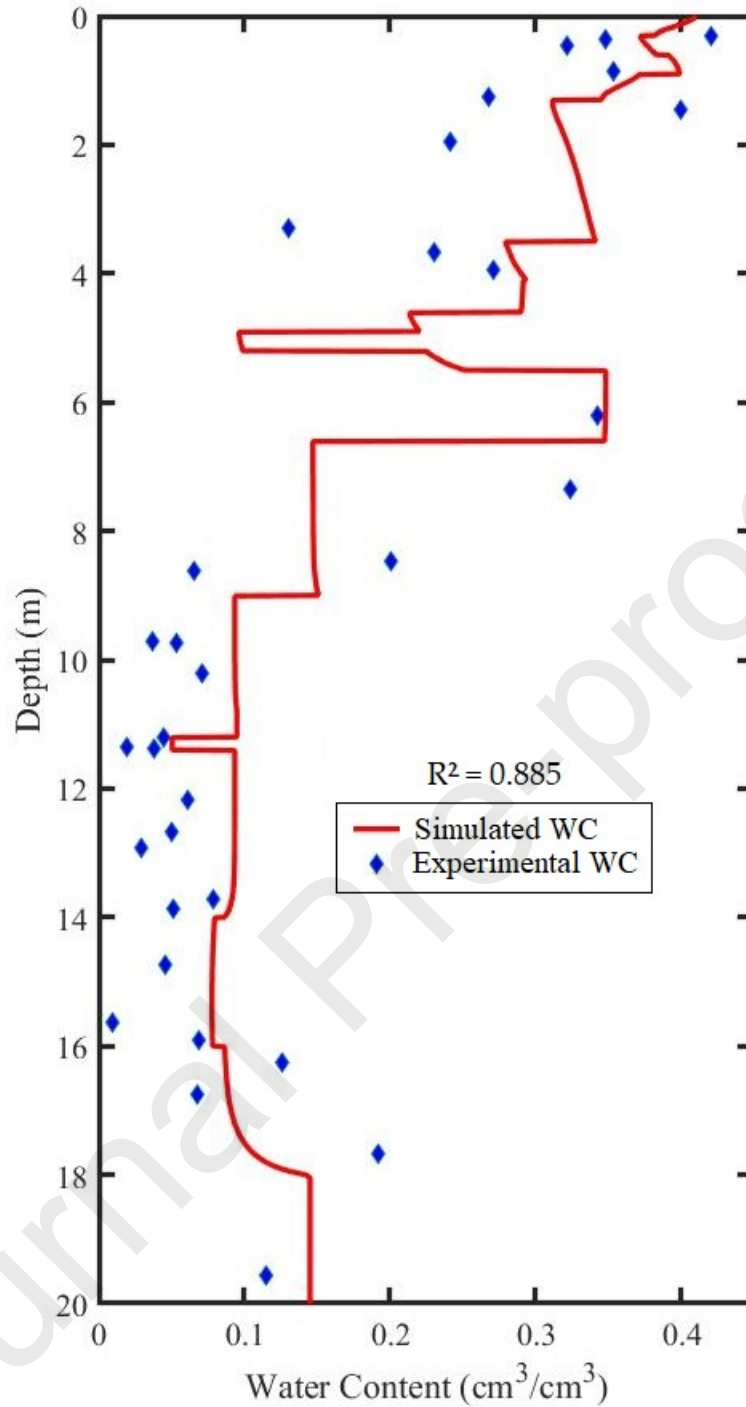


369

370 **Fig. 4.** (a) Electrical resistivity borehole data showing the ER variations in boreholes B1, B2  
 371 and B3 (23/03/2017). (b) Relative permittivity results obtained from the cross-hole GPR  
 372 profiles acquired between boreholes B1, B2 and B3 (24/01/2019).

## 373 5.2. Hydrogeology

374 As shown in Fig. 5, the simulated water content profile obtained by the model for borehole B2  
 375 (23/03/2017) showed a good agreement with experimental water content ( $R^2 > 0.885$ ) measured  
 376 at the same date. This model, which focused on the simulation of the water movement within  
 377 the matrix components of the VZ, seemed to constitute a first simplified but suitable approach  
 378 for the unidimensional simulation of water flow within the VZ of the Beauce limestone aquifer.



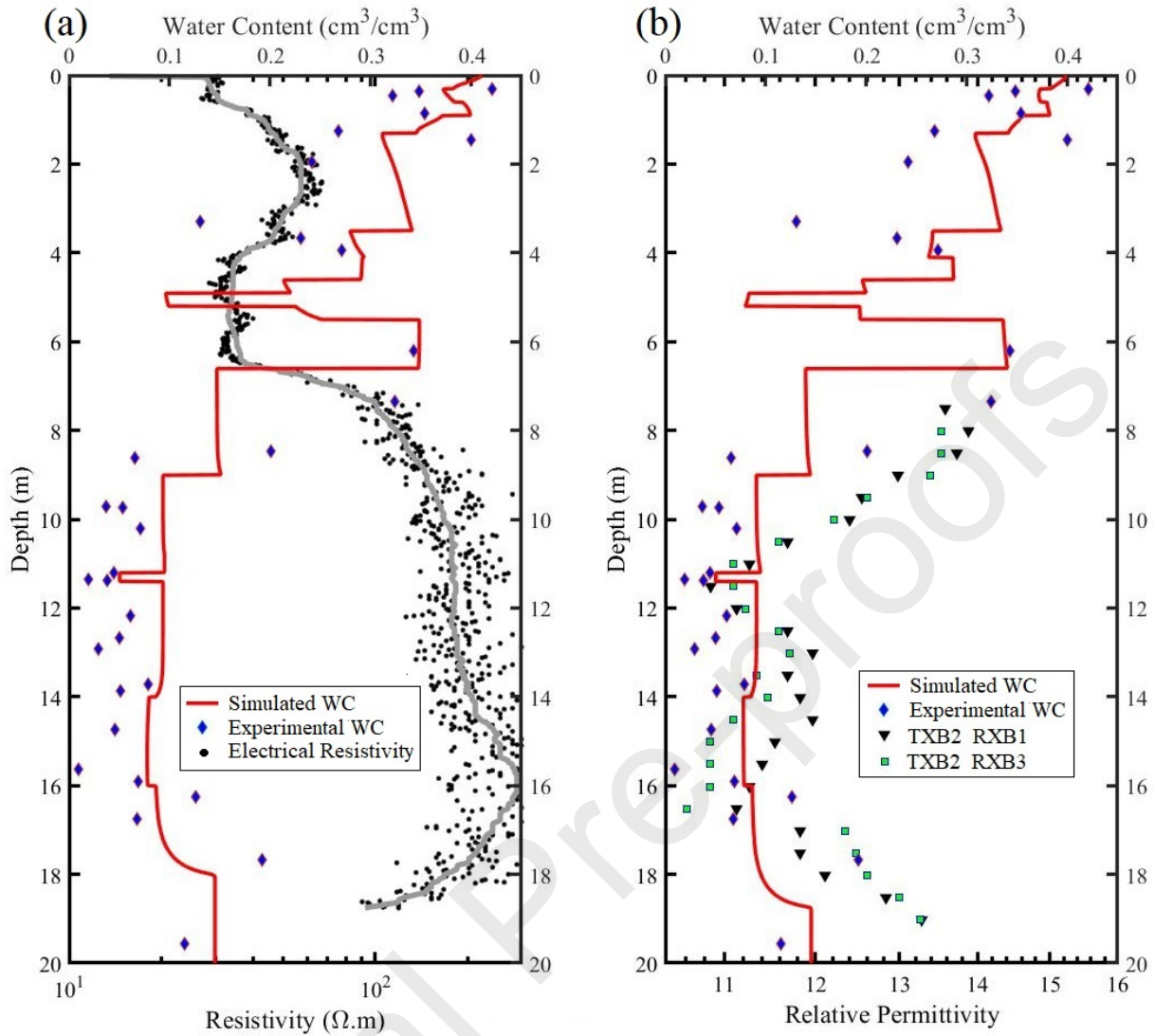
379

380 **Fig. 5** : Experimental water content (WC) plotted against the simulated water content obtained  
 381 in borehole B2 with the HYDRUS-1D software (23/03/2017).

382 The borehole ER data (23/03/2017) showed a good global correspondence with the simulated  
 383 water content distribution at the same date (Fig. 6a). This correspondence is characterized with  
 384 a global increase in the ER values along with the global decrease in the water content. This was

385 followed by a decrease in the ER values with the increase in the water content close to the water  
386 table level. Similarly, the relative permittivity data showed a good correspondence with the  
387 water content variations (Fig. 6b). A significant coherent decrease in the relative permittivity  
388 and water content was observed at a depth between 6.5 m and 9 m located at the transition zone  
389 between the incoherent limestone and the hard limestone formations. This was followed by a  
390 significant increase in the relative dielectric permittivity values along with the increase in water  
391 content close to the water table level. The water content profiles simulated for the dates of the  
392 ER (Fig. 6a) and GPR (Fig. 6b) data showed similar values with slight but noticeable  
393 differences in the top 6 meters and at a depth between 17 m and 19 m. This was expected  
394 knowing that these profiles were simulated for two close periods of the year (23<sup>rd</sup> of March and  
395 24<sup>th</sup> of January).

396 A similar pattern was observed in the three boreholes ER data and in the three dielectric  
397 permittivity profiles, which shows a good repeatability of the field geophysical data. This  
398 observation also indicates that the zones around and between the boreholes are globally and  
399 relatively homogeneous, despite the presence of local lateral heterogeneities that were observed  
400 in each of the geophysical profiles.



401

402 **Fig. 6.** (a) Borehole ER variations with respect to water content variations simulated by  
 403 HYDRUS-1D (B2, 23/03/2017), (b) Relative dielectric permittivity distribution obtained from  
 404 the GPR measurements with respect to water content variations simulated by HYDRUS-1D  
 405 (B2, 24/01/2019). The water table in borehole B2 had a depth of 18.71 m during the ER  
 406 measurements and a depth of 18.98 m during the GPR measurements.

### 407 5.3. Determination of Petrophysical Parameters

408 To determine the Archie ( $a$  and  $m$ ) and CRIM ( $\alpha$  and  $\epsilon_s$ ) petrophysical parameters, the measured  
 409 ER and relative permittivity data and the simulated water content distributions were used in the  
 410 inversion algorithm described in section 4.3.



### 411 5.3.1. Model Structure

412 As explained previously in section 4.2, the calculation was done for the part of the VZ located  
413 at a depth between 6.61 m and 19 m, where the well-cemented microcrystalline texture of the  
414 hard limestone rock along with its very low amount of fine-grained material (Aldana et al.,  
415 2021) permits the neglect of the grains surface conductivity. Therefore, the inversion model  
416 was applied on the geological unit number 3 (Table 1), which was divided into three sub-layers  
417 according to lithological description, the hydrogeological model discretization and the water  
418 content variations. Layer 1 is located at the top of the unit at a depth between 6.61 m and 9.00  
419 m. This layer, which is considered as the transition zone between the incoherent limestone ( $P_D$ )  
420 and the massive rock ( $R_B$ ) materials (Table 1), showed simulated water content variations  
421 ranging between 0.147 and 0.151  $\text{cm}^3/\text{cm}^3$  (Fig. 5). Layer 2 is located at a depth ranging  
422 between 9.01 m and 14.00 m, and is characterized by a limestone rock showing few fissures  
423 and slight alterations ( $R_D$ ) with intercalations of massive limestone rock banks ( $R_C$ ) (Mallet et  
424 al., 2022) which presented a very low porosity (Table 1). Layer 2 showed a simulated water  
425 content variation ranging between 0.050 and 0.095  $\text{cm}^3/\text{cm}^3$ . Layer 3 corresponds to the altered  
426 limestone rock that showed a highly heterogeneous structure characterized by an increased  
427 evolution towards fracturation and karstification with depth. Layer 3 is located at a depth  
428 ranging between 14.01 m and 19 m, and showed the highest water content variation with values  
429 ranging between 0.078 and 0.145  $\text{cm}^3/\text{cm}^3$ . The simulated water content values described here  
430 are those obtained for the ER measurements date (23/03/2017), while similar value ranges were  
431 also obtained for those of the GPR measurements date (24/01/2019). The inversion was carried  
432 out for each of the model's layers separately in order to investigate the effects of vertical  
433 heterogeneities on the obtained parameters. This gives us a total of 6 inversions (3 for the CRIM  
434 and 3 for the Archie's model).

### 435 5.3.2. Inversion Results

436 The inversion results of the Archie's parameters showed a value of 1.60 for the cementation  
437 exponent  $m$  in Layers 1 and 2 and a value of 1.47 in Layer 3. One can look at the cementation  
438 exponent as a measure of connectedness of the pore network which decreases as the  $m$  exponent  
439 increases (Glover, 2017). Most sediments or sedimentary rock consisting partially or  
440 completely of sand-sized fragments have cementation exponents ranging between 1.5 and 2.5  
441 (Glover et al., 1997), while lower connectedness and vuggy limestone formations are expected  
442 to be represented by higher  $m$  values. A wide range of values have been reported in the literature  
443 for limestone formations (Worthington, 1993). Values ranging between 1.6 and 2.4 have been  
444 reported for carbonates (Schön, 2004; Carothers, 1968; Hill and Milburn, 1956), while it was  
445 also suggested that they can also have higher values ranging between 2.5 and 5 due to their  
446 poorly connected pore space (Tiab and Donaldson, 2011, 2004). However, knowing that  
447 connectedness is a term which also describes the extent to which transport pathways are  
448 available, low porosity rocks characterized by relatively direct flow paths due to a well-  
449 developed fracture network could have lower values or values close to unity reflecting a fairly  
450 good connectedness provided by the fractures network. Therefore, the relatively low values  
451 obtained in our study could be related to a well-developed fracture network which is thought to  
452 be present in the study site but not fully characterized yet. Even though we used a simple  
453 porosity model that doesn't take fractures network into account in the porosity parameter, the  
454 relative effect of the fracturation could be reflected in the field resistivity data that have a major  
455 influence on the obtained  $m$  value during the inversion. Layer 3, which showed a lower  $m$  value  
456 (1.47) relative to Layers 1 and 2, has a highly heterogeneous structure characterized by  
457 increased alteration, fracturation and karstification features relative to the other layers, which  
458 might explain the relative decrease of  $m$  in this layer. Indeed, complex structural formations  
459 have been observed in the limestone VZ at the O-ZNS site (Fig. 7), where fissures, fractures  
460 and karst networks were observed at the field scale (Aldana et al., 2021). For example,

461 millimetric vugs induced by dissolution processes have been observed in the weathered rock  
 462 formations located at the water table fluctuation zone and corresponding to Layer 3. Further  
 463 dissolution episodes could have increased the vugs diameters and enhanced the permeability at  
 464 this layer. As it is evident in the Archie's equation (Eq. 7), the higher is the cementation  
 465 exponent the higher is the sensitivity of the electrical resistivity values to changes in porosity  
 466 (Ellis and Singer, 2007). The relatively similar  $m$  values that were obtained in the three layers  
 467 indicate a similar sensitivity of the electrical resistivity values to the slight differences in  
 468 porosity observed in the different layers.



469  
 470 **Fig. 7.** Images of the altered and fissured limestone formation taken while drilling the main  
 471 well at the O-ZNS observatory.

472 **Table 3.** The Archie's petrophysical parameters obtained in the three layers of the model.

Layer	Depth (m)	$a$	$m$	$n$
1	6.61-9.00	0.80	1.60	2.00
2	9.01-14.00	0.70	1.60	2.00
3	14.01-19.00	0.60	1.47	2.00

473  
 474 The inversion results showed a value of 0.8 for the parameter  $a$  in layer 1, while it showed a  
 475 value of 0.7 and 0.6 in layers 2 and 3 respectively. Even though no real correlation was found  
 476 between this parameter and tortuosity or lithology,  $a$  is an empirical constant which is believed  
 477 to have a role in the compensation for systematic errors in the porosity, electrical resistivity or  
 478 pore fluid resistivity measurements (Glover, 2016, 2015). This empirical factor which appeared

479 in the Winsauer et al. (1952) modification of the Archie's first law usually provided improved  
480 fits with experimental data, especially when dealing with low-quality and sparse types of  
481 datasets. It is commonly assumed that the size of  $a$  is a measure of the extent to which an overall  
482 systematic error is present in the measurements. Recent research suggested that these errors  
483 produce non-unity values of  $a$ , while the closer this parameter is to unity, the better is the data  
484 quality. Additionally,  $a$  has an important role in the calculation of a more accurate  $m$  value,  
485 since it compensates for the experimental errors present in the parameters used to calculate  $m$   
486 during the fitting procedure (Glover, 2016). Throughout the inversion,  $a$  takes the appropriate  
487 fitted value to compensate for the presence of systematic errors and reduce their effects on the  
488 obtained  $m$  value. Therefore, the value of  $a$  obtained from the fit can be considered as an  
489 empirical parameter that describes the accuracy of the measured data in the Archie equation.  
490 The observed decreasing behavior value of  $a$ , from 0.8 in layer 1 to 0.6 in layer 3 could be  
491 attributed to the increase in the measurements errors associated with the evolution of alteration,  
492 fracturation and karstification with depth. This phenomenon can increase the medium  
493 heterogeneities and produce errors in the field measurements which the fitted value of  $a$   
494 compensated for during the inversion. Even though  $a$  was not shown to have an underlying  
495 physical meaning, few studies suggested  $a$  values ranging between 0.4 and 2.3 in the case of  
496 limestone formations (Timur et al., 1972; Porter and Carothers, 1970; Carothers, 1968). In  
497 accordance with our inversion results, the most recent studies reported values of  $a$  ranging  
498 between 0.2 and 1.8 for limestone formations (Glover, 2016, 2015).

499 The inversion of the CRIM showed a  $\epsilon_s$  value of 7.99 in Layer 1, 7.97 in Layer 2 and 8.00 in  
500 Layer 3.  $\epsilon_s$  is mainly influenced by the mineralogy and rock formation characteristics.  
501 Therefore, similar values were expected to be observed in the three layers, knowing that they  
502 are all considered as part of the limestone rock main geological unit (Table 1). However, the  
503 slight differences in the  $\epsilon_s$  values observed in the three layers can be attributed to the differences

504 in the geological characteristics of the layers in terms of materials heterogeneity and degree of  
 505 alteration which evolved with depth. Nevertheless, these slight differences, as small as they are,  
 506 could also be simply induced by the mathematical procedure of the inversion. In accordance  
 507 with our results, values ranging between 4 and 13 have been reported in the literature for the  
 508 solid phase dielectric permittivity of limestone formations, which is considered as one of the  
 509 main sources of uncertainties in the electromagnetic waves application of the CRIM model  
 510 (Mount and Comas, 2014; Reynolds, 2011; Cassidy, 2009).

511 The inversion of the CRIM showed an  $\alpha$  value of 0.50 in Layer 1, 0.58 in Layer 2 and 0.61 in  
 512 Layer 3. Values ranging between -1 and 1 were reported for  $\alpha$  over the last few decades, which  
 513 is a geometrical factor connecting the effective layering direction of the components to the  
 514 applied electric field direction (West et al., 2003; Knoll, 1996; Roth et al., 1990). Several GPR  
 515 studies indicated that most geological facies can take an  $\alpha$  value of 0.5 (West et al., 2003; Knoll,  
 516 1996). Values ranging between 0.46 and 0.65 have been previously obtained during laboratory  
 517 measurements (Mount and Comas, 2014; Moysey and knight, 2004).

518 **Table 4.** The CRIM's petrophysical parameters obtained in the model layers.

Layer	Depth (m)	$\alpha$	$\epsilon_s$
1	6.61-9.00	0.50	7.99
2	9.01-14.00	0.58	7.97
3	14.01-19.00	0.61	8.00

519 This approach was shown to produce acceptable results reflected in a very good fit between the  
 520 measured and calculated data in the three layers, and with values that generally fall in the ranges  
 521 reported in previous studies. The degree of accuracy of this approach is defined by the  
 522 resolution of the hydrogeological model and its capability in capturing the VZ water content  
 523 variations. The water content distribution is strongly influenced by the extent of heterogeneities  
 524 incorporated in the hydrogeological model and in the porosity parameter of the empirical

relationships, especially in limestone formations with complex porosity patterns. Characterizing the impact of the observed fissures and fractures networks on the water flow at the field scale of the O-ZNS VZ is indeed crucial. Therefore, our future work is focused on the development of a precise description of the water flow through the whole porosity of this highly heterogeneous VZ by combining 3D experimental observations and numerical simulations with dual-porosity or dual-permeability approaches. This will form the basis to incorporate the complex multiple porosity patterns in the petrophysical relationships in order to provide an improved estimation of petrophysical parameters. The geological heterogeneities encountered at different study sites might explain the wide range of values reported in the literature for the Archie's and CRIM's parameters, especially in carbonate geology environments, which are complex mediums that can develop different porosity patterns, fractures networks and flow paths.

## 6. Conclusion

This study attempted to investigate the relationship between geophysical properties and water content distribution, and determine the Archie's and CRIM's petrophysical parameters by integrating ER and dielectric permittivity data with simulated water content data at the scale of a highly heterogeneous limestone VZ. The simulated and experimental hydrogeological data displayed a very good correspondence with the geophysical data reflected in coherent variations in water content, ER and relative permittivity. These observations showed a significant sensibility of geophysical methods to water content variations, and demonstrated the potential of these methods in investigating hydrogeological processes at our study site.

The inversion results of the Archie model showed values ranging between 0.6 and 0.8 for  $a$  and between 1.47 and 1.60 for  $m$ . On the other hand, the inversion results of the CRIM showed values ranging between 0.50 and 0.61 for  $\alpha$  and between 7.97 and 8.00 for  $\epsilon_s$ . Similar results

549 were obtained in the three model layers, with slight differences that were attributed to the  
550 vertical heterogeneities of the limestone rock formation (e.g., degree of alteration, fracturation,  
551 karstification). This observation demonstrates the sensitivity of petrophysical parameters to  
552 vertical geological heterogeneities that should be taken into account when calculating these  
553 parameters. Given the ranges of variability used in the inversion, the obtained values are within  
554 the bounds of values found in the literature, where a wide range have been reported for  
555 carbonate formations due to their complex geological features that might vary greatly among  
556 different study sites.

557 Throughout this study, the petrophysical parameters were successfully obtained with a very  
558 good fit between the measured and simulated data. However, the demonstrated approach  
559 showed an important sensitivity to the resolution of water content variations captured by the  
560 used hydrogeological model, and to the geological heterogeneities of the medium. Therefore,  
561 the perspectives include further improvements to this approach by conducting extensive studies  
562 at larger scales, and combining 3D experimental observations and numerical simulations using  
563 dual-porosity and dual-permeability modeling approaches that can capture the water content  
564 and geological heterogeneities at a higher resolution in complex and fractured limestone  
565 formations. In this context, our future work is focused on the development of a geological model  
566 constrained by laboratory calibrations that can give a better estimation of the limestone complex  
567 porosity patterns to be incorporated in the hydrogeological model and empirical relationships.

## 568 **Acknowledgment**

569 This study was conducted within the framework of the O-ZNS project which is part of the  
570 PIVOTS program (<https://plateformes-pivots.eu/o-zns/?lang=en>). We gratefully acknowledge  
571 the financial support provided to the PIVOTS project by the Région Centre–Val de Loire (ARD  
572 2020 program and CPER 2015-2020), and by the French Ministry of Higher Education and

573 Research. This research work is co-funded by the Labex Voltaire (ANR-10-LABX-100-01) and  
574 by the European Union with the European Regional Development Fund (FEDER) in Centre-  
575 Val de Loire. Data can be obtained upon request to the corresponding author. In addition, the  
576 data will be soon available on an O-ZNS data repository with their own DOI.

## 577 **References**

- 578 Abbar, B., Isch, A., Michel, K., Abbas, M., Vincent, H., Abbasimaedeh, P., & Azaroual, M.  
579 (2021). Fiber optic technology for environmental monitoring: state of the art and  
580 application in the observatory of transfers in the vadose zone (O-ZNS). Chapter book in  
581 “Instrumentation and Measurement Technologies for Water Cycle Management”,  
582 Springer (Wiley). <https://link.springer.com/book/9783031082610>.
- 583 Abbas, M., Jardani, A., Soueid Ahmed, A., Revil, A., Brigaud, L., Bégassat, Ph., & Dupon, J.  
584 P. (2017). Redox potential distribution of an organic-rich contaminated site obtained by  
585 the inversion of self-potential data. *Journal of Hydrology*. 554,111–127.  
586 <https://doi.org/10.1016/j.jhydrol.2017.08.053>.
- 587 Ahmed, A. S., Jardani, A., Revil, A., & Dupont, J. P. (2014). Hydraulic conductivity field  
588 characterization from the joint inversion of hydraulic heads and self-potential data.  
589 *Water Resources Research* . 50, 3502–3522. <https://doi.org/10.1002/2013WR014645>.
- 590 Aldana, C., Isch, A., Bruand, A., Azaroual, M., & Coquet., Y. (2021). Relationship between  
591 hydraulic properties and material features in a heterogeneous vadose zone of a  
592 vulnerable limestone aquifer. *Vadose Zone Journal*. e20127.  
593 <https://doi.org/10.1002/vadosezonej2.20127>.
- 594 Ammar, A. & Kamal, K. A. (2017). Resistivity method contribution in determining of fault  
595 zone and hydro-geophysical characteristics of carbonate aquifer, eastern desert, Egypt.  
596 *Applied Water Science*. <https://doi.org/10.1007/s13201-017-0639-9>.
- 597 Archie, G. E. (1942). The electrical resistivity log as an aid in determining some reservoir  
598 characteristics. *Transactions of American Institute of Mining Metallurgical Engineers*.  
599 146. 54-62. <https://doi.org/10.2118/942054-G>.



- 600 Arora, B., Dwivedi, D., Faybishenko, B., Jana, R., & Wainwright, H. (2019). Understanding  
601 and Predicting Vadose Zone Processes. *Reviews in Mineralogy*, 85.  
602 <https://doi.org/10.1515/9781501512001-011>.
- 603 Birchak, J. R., Gardner, C. G., Hipp, J. E., & Victor, J. M. (1974). High dielectric constant  
604 microwave probes for sensing soil moisture. *IEEE*, 62: 93-98. doi:  
605 10.1109/PROC.1974.9388.
- 606 Binley, A., Winship, P., Middleton, R., Pokar, M., & West, J. (2001). High-resolution  
607 characterization of vadose zone dynamics using crossborehole radar. *Water Resources*  
608 *Research*. 37(11), 2639–2652. <https://doi.org/10.1029/2000WR000089>.
- 609 Binley, A., Cassiani, G., Middleton, R., & Winship, P. (2002a). Vadose zone flow model  
610 parameterisation using cross-borehole radar and resistivity imaging. *Journal of*  
611 *Hydrology*. 267:147–159. [https://doi.org/10.1016/S0022-1694\(02\)00146-4](https://doi.org/10.1016/S0022-1694(02)00146-4).
- 612 Binley, A., Cassiani, G., & Deiana, R. (2010). Hydrogeophysics - Opportunities and  
613 Challenges. *Bollettino di Geofisica Teorica ed Applicata*, 51. 267-284.
- 614 Binley, A., Hubbard, S. S., Huisman, J. A., Revil, A., Robinson, D. A., Singha, K., & Slater, L.  
615 D. (2015). The emergence of hydrogeophysics for improved understanding of  
616 subsurface processes over multiple scales. *Water Resources Research*. 51. 3837–3866.  
617 <https://doi.org/10.1002/2015WR017016>.
- 618 Blazevic, L., Bodet, L., Pasquet, S., Linde, N., Jougnot, D., Longuevergne, L. (2020). Time-  
619 Lapse Seismic and Electrical Monitoring of the Vadose Zone during A Controlled  
620 Infiltration Experiment at the Ploemeur Hydrological Observatory, France. *Water*. 12.  
621 10.3390/w12051230.
- 622 Brunet, P., Clément, R., & Bouvier, C. (2010). Monitoring soil water content and deficit using  
623 Electrical Resistivity Tomography (ERT) – A case study in the Cevennes area, France.  
624 *Journal of Hydrology*, 380. 146-153. <https://doi.org/10.1016/j.jhydrol.2009.10.032>.
- 625 Buchner, R., Barthel, J., & Stauber, J. (1999). The dielectric relaxation of water between 0°C  
626 and 35°C. *Chemical Physics Letters*. 306(1–2), 57– 63. [https://doi.org/10.1016/S0009-](https://doi.org/10.1016/S0009-2614(99)00455-8)  
627 [2614\(99\)00455-8](https://doi.org/10.1016/S0009-2614(99)00455-8).
- 628 Carothers, J. E. (1968). A statistical study of the formation factor relation. *The Log Analyst* 9  
629 (5). 13-20 .

- 630 Cassiani, G., Ferraris, S., Giustiniani, M., Deiana, R., & Strobba, C. (2009b). Time-lapse  
631 surface-to-surface GPR measurements to monitor a controlled infiltration experiment.  
632 *Bollettino di Geofisica Teorica ed Applicata*. 50. 209-226.
- 633 Cassidy, N. (2009). Ground Penetrating Radar Data Processing, Modelling and Analysis.  
634 <https://doi.org/10.1016/B978-0-444-53348-7.00005-3>.
- 635 Chan, C. Y., & Knight; R. J. (2001). Laboratory measurements of electromagnetic wave  
636 velocity in layered sands, *Water Resources Research*, 37(4), 1099–1105,  
637 doi:10.1029/2000WR900356.
- 638 Chan, C. Y., & Knight; R. J. (1999). Determining water content and saturation from dielectric  
639 measurements in layered materials. *Water Resources Research*. 35. 85-93.  
640 doi/pdf/10.1029/1998WR900039.
- 641 Dafflon, B., Irving, J., & Barrash, W. (2011). Inversion of multiple intersecting high-resolution  
642 crosshole GPR profiles for hydrological characterization at the Boise hydrogeophysical  
643 research site. *Journal of Applied Geophysics*. 73:305–314.  
644 <https://doi.org/10.1016/j.jappgeo.2011.02.001>.
- 645 De Jong, S., Heijenk, R., Nijland, W., & Meijde, M. (2020). Monitoring Soil Moisture  
646 Dynamics Using Electrical Resistivity Tomography under Homogeneous Field  
647 Conditions. *Sensors (Basel, Switzerland)*. 20(18). 5313. [https://doi.org/ 20.](https://doi.org/10.3390/s20185313)  
648 [10.3390/s20185313](https://doi.org/10.3390/s20185313).
- 649 Eching, S. O., Hopmans, J. W., & Wendroth, O. (1994). Unsaturated hydraulic conductivity  
650 from transient multistep outflow and soil water pressure data. *Soil science society of*  
651 *America journal* 58(3): 687–695.
- 652 Ellis, D. V., & Singer, J. M. (2007). *Well Logging for Earth Scientists*. Vol. 692, Springer,  
653 Dordrecht.
- 654 Evett, S. (2003). Soil Water Measurement by Time Domain Reflectometry. In *Encyclopedia of*  
655 *Water Science*; Marcel Dekker, Inc.: New York, NY, USA; ISBN 0-8247-4241-9.
- 656 Evett, S. (2008). Neutron moisture meters. *Field Estimation of Soil Water Content: A Practical*  
657 *Guide to Methods, Instrumentation, and Sensor Technology*. 39-54. ISSN 1018–5518.
- 658 Gardner, W. R. (1956). Calculation of Capillary Conductivity from Pressure Plate Outflow  
659 Data. 317–320p.

- 660 Garré, S., Hyndman, D., Mary, B., and Werban, U. (2021). Geophysics conquering new  
661 territories: The rise of Agrogeophysics. *Vadose Zone Journal*. p. e20115.  
662 <https://doi.org/10.1002/vzj2.20115>.
- 663 Gance, J., Malet, J. P., Supper, R., Sailhac, P., Ottowitz, D., & Jochum, B. (2016). Permanent  
664 electrical resistivity measurements for monitoring water circulation in clayey landslides.  
665 *Journal of Applied Geophysics*. 126, 28-115.  
666 <https://doi.org/10.1016/j.jappgeo.2016.01.011>.
- 667 Glover, P. W. J., Gomez, J. B., Meredith, P. G., Hayashi, K., Sammonds, P. R., & Murrell, S.  
668 A. F. (1997). Damage of saturated rocks undergoing triaxial deformation using complex  
669 electrical conductivity measurements: experimental results: *Physics and Chemistry of*  
670 *the Earth*, 22, no. 1–2, 57–61. doi: 10.1016/S0079-19469700078-5.
- 671 Glover, P. W. J. (2009). What is the cementation exponent? A new interpretation. *The Leading*  
672 *Edge*, 28, 82–85. <https://doi.org/10.1190/1.3064150>.
- 673 Glover, P. W. J. (2010). A generalised Archie's law for n phases. *Geophysics*. 75, E247–E265.  
674 <https://doi.org/10.1190/1.3509781>, 2010.
- 675 Glover, P. W. J. (2015). Geophysical properties of the near surface Earth: Electrical properties.  
676 *Treatise on Geophysics*, 11, 89–137, 2015. [https://doi.org/10.1016/B978-0-444-53802-](https://doi.org/10.1016/B978-0-444-53802-4.00189-5)  
677 [4.00189-5](https://doi.org/10.1016/B978-0-444-53802-4.00189-5).
- 678 Glover, P. (2016). Archie's law – a reappraisal: *Solid Earth*. 7. 1157-1169.  
679 <https://doi.org/10.5194/se-7-1157-2016>.
- 680 Glover, P. W. J. (2017). A new theoretical interpretation of Archie's saturation exponent. *Solid*  
681 *Earth*. 8. 805-816. <https://doi.org/10.5194/se-8-805-2017>.
- 682 Griffiths, D. H., Barker, R. D. (1993). Two-dimensional resistivity imaging and modeling in  
683 areas of complex geology. *Journal of Applied Geophysics*. 29. 211–226.
- 684 Hagrey, S. (2007). Geophysical imaging of root-zone, trunk, and moisture heterogeneity.  
685 *Journal of experimental botany*. 58. 839-54. <https://doi.org/10.1093/jxb/erl237>.
- 686 He, H., Aogu, K., Li, M., Xu, J., Sheng, W., Jones, S.B., González-Teruel, J.D., Robinson,  
687 D.A., Horton, R., Bristow, K., Dyck, M., Filipović, V., Noborio, K., Wu, Q., Jin, H.,  
688 Feng, H., Si, B., & Lv, J. (2021). Chapter Three - A review of time domain reflectometry

- 689 (TDR) applications in porous media. In: D.L. Sparks (Ed.). *Advances in Agronomy*.  
690 Academic Press. 83-155. <https://doi.org/10.1016/bs.agron.2021.02.003>.
- 691 Hendrickx, J. M. H., Das, B., Corwin, D. L., Wraith, J. M., & Kachanoski, R. G. (2002).  
692 Relationship between soil water solute concentration and apparent soil electrical  
693 conductivity. In Dane, J. H., Topp, G.C. (Eds.), *Methods of Soil Analysis: Part 4.*  
694 *Physical Methods*. Soil Science Society of America, Madison, WI, USA. 1275–1282.
- 695 Herkelrath, W. N., Hamburg, S. P., & Murphy, F. (1991). Auto- matic, real-time monitoring of  
696 soil moisture in a remote field area with time domain re- flectometry. *Water Resources*  
697 *Research*. 27, 857- 864.
- 698 Hill, H. J., & Milburn, J. D. (1956). Effect of clay and water salinity on electrochemical  
699 behaviour of reservoir rocks. *Petroleum Transactions*. 207. 65–72.  
700 <https://doi.org/10.2118/532-G>.
- 701 Hubbard, S. S., Chen, J. S., Peterson, J., Majer, E. L., Williams, K., Swift, D. J., Mailloux, B.,  
702 & Rubin, Y. (2001a). Hydrogeological characterization of the South Oyster Bacterial  
703 Transport Site using geophysical data. *Water Resources Research*. 37(10). 2431–2456.  
704 <https://doi.org/10.1029/2001WR000279>.
- 705 Huisman, J. A., Hubbard, S. S., Redman, J. D., & Annan, P. A. (2003), Measuring soil water  
706 content with ground penetrating radar: A review. *Vadose Zone Journal*. 2(4). 476–491.  
707 <https://doi.org/10.2113/2.4.476>.
- 708 Isch, A., Montenach, D., Hammel, F., Ackerer, P., Coquet, Y (2019). A Comparative Study of  
709 Water and Bromide Transport in a Bare Loam Soil Using Lysimeters and Field Plots.  
710 *Water*. 11. 1199. <https://doi.org/10.3390/w11061199>.
- 711 Isch, A., Coquet, Y., Abbar, B., Aldana, B., Abbas, M., Bruand, A., Azaroual, M. (2022). A  
712 comprehensive experimental and numerical analysis of water flow and travel time in a  
713 highly heterogeneous vadose zone. *Journal of Hydrology*. 610. 127875.  
714 <https://doi.org/10.1016/j.jhydrol.2022.127875>.
- 715 Jardani, A., Revil, A., & Dupont, J. P. (2012). Stochastic joint inversion of hydrogeophysical  
716 data for salt tracer test monitoring and hydraulic conductivity imaging. *Advances in*  
717 *Water Resources*. 52. 62-77. <https://doi.org/10.1016/j.advwatres.2012.08.005>.
- 718 Johnson, T. C., Versteeg, R. J., Ward, A., Day-Lewis, F. D., & Revil, A. (2010). Improved  
719 hydrogeophysical characterization and monitoring through parallel modeling and

- 720 inversion of time-domain resistivity and induced-polarization data. *Geophysics*. 75. 27-  
721 41. <https://doi.org/10.1190/1.3475513>.
- 722 Johnson, T., Versteeg, R., Thomle, J., Hammond, G., Chen, X., & Zachara, J. (2015). Four-  
723 dimensional electrical conductivity monitoring of stage-driven river water intrusion:  
724 Accounting for water table effects using a transient mesh boundary and conditional  
725 inversion constraints. *Water Resources Research*. 51. 6177–6196.  
726 <https://doi.org/10.1002/2014WR016129>.
- 727 Klotzsche, A., Jonard, F., Looms, M. C., Van Der Kruk, J., & Huisman, J. A. (2018). Measuring  
728 soil water content with ground penetrating radar: A decade of progress. *Vadose Zone*  
729 *Journal*. 17:180052. <https://doi.org/10.2136/vadosezonej2018.03.0052>.
- 730 Klotzsche, A., L ¨arm, L., Vanderborght, J., Cai, G., Morandage, S., Z ¨orner, M. (2019).  
731 Monitoring soil water content using time lapse horizontal borehole GPR data at the field  
732 plotscale. *Vadose Zone Journal*. 18. 190044. <https://doi.org/10.2136/vzj2019.05.0044>.
- 733 Klotzsche, A., Van Der Kruk, J., Linde, N., Doetsch, J., & Vereecken, H. (2013). 3-D  
734 characterization of high-permeability zones in a gravel aquifer using 2-D crosshole GPR  
735 full-waveform inversion and wave guide detection. *Geophysical Journal International*.  
736 195:932–944. <https://doi.org/10.1093/gji/ggt275>.
- 737 Kowalsky, M., Finsterle, S., Peterson, J., Hubbard, S., Rubin, Y., Majer, E., Ward, A., & Gee,  
738 G. (2005). Estimation of field-scale soil hydraulic and dielectric parameters through  
739 joint inversion of GPR and hydrological data. *Water Resources Research*., 41, W11425,  
740 <https://doi.org/10.1029/2005WR004237>.
- 741 Linde, N., Binley, A., Tryggvason, A., Pedersen, L. B., & Revil, A. (2006). Improved hydro-  
742 geophysical characterization using joint inversion of cross-hole electrical resistance and  
743 ground-penetrating radar traveltime data. *Water Resources Research*. 42. W12404.  
744 <https://doi.org/10.1029/2006WR005131>.
- 745 Looms, M. C., Binley, A., Jensen, K. H., Nielsen, L., & Hansen, T. M. (2008a). Identifying  
746 unsaturated hydraulic parameters using an integrated data fusion approach on cross-  
747 borehole geophysical data. *Vadose Zone Journal*. 7. 238–248.  
748 <https://doi.org/10.2136/vadosezonej2007.0087>.

- 749 Looms, M. C., Jensen, K. H., Binley, A., & Nielsen, L. (2008b). Monitoring Unsaturated Flow  
750 and Transport Using Cross-Borehole Geophysical Methods. *Vadose Zone Journal*. 7.  
751 227–237. <https://doi.org/10.2136/vadosezonej2007.0087>.
- 752 Lucia, F. J. (2007). *Carbonate Reservoir Characterization: An Integrated Approach*. Springer.  
753 <https://link.springer.com/book/10.1007/978-3-540-72742-2>
- 754 Lunt, I., Hubbard, S. S., & Rubin, Y. (2005). Soil moisture estimation using ground-penetrating  
755 radar reflection data. *Journal of Hydrology*. 307. 254–269.  
756 <https://doi.org/10.1016/j.jhydrol.2004.10.014>.
- 757 Mallet, C., Isch, A., Laurent, G., Jodry, C., Azaroual, M. (2022). Integrated static and dynamic  
758 geophysical and geomechanical data for characterization of transport properties.  
759 *International Journal of Rock Mechanics and Mining Sciences*. 153.  
760 <https://doi.org/10.1016/j.ijrmms.2022.105050>.
- 761 Mallet, C., Jodry, C., Isch, A., Laurent, G., Deparis, J. & Azaroual, M. (2021). Multi-  
762 geophysical field measurements to characterize lithological and hydraulic properties of  
763 a multi-scale karstic and fractured limestone vadose zone: Beauce aquifer (O-ZNS).  
764 Chapter book in: *Instrumentation and Measurement Technologies for Water Cycle*  
765 *Management*, Springer. <https://link.springer.com/book/9783031082610>.
- 766 Mary, B., Peruzzo, L., Boaga, J., Schmutz, M., Wu, Y., Hubbard, S., & Cassiani, G. (2018).  
767 Small scale characterization of vine plant root water uptake via 3D electrical resistivity  
768 tomography and Mise-à-la-Masse method. *Hydrology and Earth System Sciences*. 22.  
769 5427-5444. <https://doi.org/10.5194/hess-22-5427-2018>.
- 770 Mohamed, A., & Hamada, G. (2017). Determination Techniques of Archie's Parameters: a, m  
771 and n in Heterogeneous Reservoirs. *Journal of Geophysics and Engineering*. 14.  
772 <https://doi.org/10.1088/1742-2140/aa805c>.
- 773 Mount, G. J., & Comas, X. (2014). Estimating porosity and solid dielectric permittivity in the  
774 Miami Limestone using high-frequency ground penetrating radar (GPR) measurements  
775 at the laboratory scale. *Water Resources Research*. 50, 7590–7605.  
776 <https://doi.org/10.1002/2013WR014947>.
- 777 Mualem, Y. (1976.) A new model for predicting the hydraulic conductivity of unsaturated  
778 porous media. *Water Resources Research*. 12(3). 513–522.  
779 <https://doi.org/10.1029/WR012i003p00513>.

- 780 Moysey, S., & Knight, R. J. (2004). Modeling the field-scale relationship between dielectric  
781 constant and water content in heterogeneous systems. *Water Resources Research*.40.  
782 W03510, doi:10.1029/2003WR002589.
- 783 Nimmo, J. R. (2005). Unsaturated Zone Flow Processes. *Encyclopedia of Hydrological*  
784 *Sciences*, Wiley, Chichester, UK. 2299–2322.
- 785 Knoll, M. D., (1996). A petrophysical basis for Ground-penetrating radar and very early time  
786 electromagnetics, electrical properties of sand-clay mixtures. Unpublished Ph.D.  
787 dissertation, University of British Columbia, 316 p.
- 788 Paz, C., Alcalá, F. J., Carvalho, J. M., & Ribeiro, L. (2017). Current uses of ground penetrating  
789 radar in groundwater-dependent ecosystems research. *Science of The Total*  
790 *Environment*., 595. 868–885. <https://doi.org/10.1016/j.scitotenv.2017.03.210>.
- 791 Porter, C. R. & Carothers, J. E. (1970). Formation factor porosity relation derived from well  
792 log data, *Trans. SPWLA 11<sup>th</sup> Ann. Logging Symp.*, 1–19, 1970.
- 793 Reynolds, J. (2011). *An Introduction to Applied and Environmental Geophysics*. Wiley. ISBN:  
794 978-0-471-48535-3.
- 795 Richards, L.A., 1931. Capillary conduction of liquids through porous mediums. *J. Appl. Phys.*  
796 1, 318–333. <https://doi.org/10.1063/1.1745010>.
- 797 Robinson, D., Jones, S., Wraith, J., Or, D., & Friedman, S. (2003). A review of advances in  
798 dielectric and electrical conductivity measurement in soils using time domain  
799 reflectometry, *Vadose Zone Journal*. 2. 444–475. <https://doi.org/10.2113/2.4.444>.
- 800 Robinson, D., Binley, A., Crook, N., Day-Lewis, F., Ferré, T., Grauch, V.J.S, Knight, R., Knoll,  
801 M., Lakshmi, V., Miller, R., Nyquist, J., Pellerin, L., Singha, K., & Slater, L. (2008).  
802 Advancing process-based watershed hydrological research using near-surface  
803 geophysics: A vision for, and review of, electrical and magnetic geophysical methods.  
804 *Hydrological Processes – Wiley*. 22. 3604–3635. <https://doi.org/10.1002/hyp.6963>.
- 805 Roth, K., Schulin, R., Fluhler, H., & Attinger, W. (1990). Calibration of time domain  
806 reflectometry for water content measurement using a composite dielectric approach.  
807 *Water Resources Research*. 26. 2267–2273.  
808 <https://doi.org/10.1029/WR026i010p02267>.
- 809 Rubin, Y., & Hubbard, S. S. (2005). *Hydrogeophysics*, 523 pp., Springer, N. Y.

- 810 Rust, C. F. (1952). Electrical Resistivity Measurements on Reservoir Rock Samples by the  
811 Two-Electrode and Four-Electrode Methods. AIME Transactions, 195. 217-224.
- 812 Schön, J. H. (2004). Physical Properties of Rocks: Fundamentals and Principles of  
813 Petrophysics. Edited by: Helbig, K. and Treitel, S., Vol.18, Amsterdam, the  
814 Netherlands: Elsevier, ISBN: 008044346X, 2004.
- 815 Šimůnek, J., van Genuchten, M.T., & Šejna, M. (2016). Recent Developments and Applications  
816 of the HYDRUS Computer Software Packages. Vadose Zone Journal. 15(7).  
817 <https://doi.org/10.2136/vadosezonej2016.04.0033>.
- 818 Skierucha, W., Wilczek, A., Szyplowska, A., Sławiński, C., Lamorski, K., Skierucha, W.,  
819 Wilczek, A., Szyplowska, A., Sławiński, C., & Lamorski, K. (2012). A TDR-based soil  
820 moisture monitoring system with simultaneous measurement of soil temperature and  
821 electrical conductivity. Sensors, 12. 13545–13566. <https://doi.org/10.3390/s121013545>.
- 822 Steelman, C., & Endres, A. (2011). Comparison of Petrophysical Relationships for Soil  
823 Moisture Estimation using GPR Ground Waves. Vadose Zone Journal. 10. 270.  
824 <https://doi.org/10.2136/vadosezonej2010.0040>.
- 825 Stephens, D. B. (2019). Vadose Zone Hydrology. CRC Press, 347 Pages. ISBN  
826 9780367448783.
- 827 Sweeney, S. A. & Jennings, H. Y. (1960). The electrical resistivity of preferentially water-wet  
828 and preferentially oil-wet carbonate rock. Producers Monthly. 24 (7). 29-32, 1960.
- 829 Tiab, D., & Donaldson, E. C. (2004). Petrophysics: Theory and Practice of Measuring Reservoir  
830 Rock and Fluid Transport Properties: Second Edition. Gulf Professional Publishing –  
831 Elsevier. ISBN: 9780080497655
- 832 Timur, A., Hemkins, W. B., & Worthington, A. E. (1972). Porosity and pressure dependence  
833 of formation resistivity factor for sandstones. Trans. CWLS 4<sup>th</sup> Formation Evaluation  
834 Symp., 30 pp.
- 835 Topp, G. C., Davis, J. L., & Annan, A. P. (1980). Electromagnetic determination of soil water  
836 content: Measurements in coaxial transmission lines. Water Resources Research.  
837 16.574–582. <https://doi.org/10.1029/WR016i003p00574>.



- 838 van Genuchten, M. T. (1980). A closed-form equation for predicting the hydraulic conductivity  
839 of unsaturated soils. *Soil Science Society of America Journal*. 44(5). 892–898.  
840 <https://doi.org/10.2136/sssaj1980.03615995004400050002x>.
- 841 van Genuchten, M. T., Leij, F. J., & Yates, S. R. (1991). The RetC code for quantifying  
842 hydraulic functions of unsaturated soils. EPA/600/2-91/065, R.S. 83.
- 843 Verhoef, A., Fernández-Gálvez, J., Diaz-Espejo, A., Main, B.E. & El-Bishti, M. (2006). The  
844 diurnal course of soil moisture as measured by various dielectric sensors: Effects of soil  
845 temperature and the implications for evaporation estimates. *Journal of Hydrology*. 321.  
846 147-162. <https://doi.org/10.1016/j.jhydrol.2005.07.039>.
- 847 Vereecken, H., Binley, A., Cassiani, G., Revil, A., & Titov, K. (2006). *Applied*  
848 *Hydrogeophysics*, 383 pp., Springer, Dordrecht, Netherlands.
- 849 Vilhelmsen, T. N., Behroozmand, A. A., Christensen, S. & Nielsen, T. H. (2014). Joint  
850 inversion of aquifer test, MRS, and TEM data. *Water Resources Research*. 50. 3956–  
851 3975. <https://doi.org/10.1002/2013WR014679>.
- 852 Wehrer, M., & Slater, L. (2015). Characterization of water content dynamics and tracer  
853 breakthrough by 3-D electrical resistivity tomography (ERT) under transient  
854 unsaturated conditions. *Water Resources Research*. 51.  
855 <https://doi.org/10.1002/2014WR016131>.
- 856 West, L. J., Huang, Y., & Handley, K. (2001). Dependence of Sandstone Dielectric Behaviour  
857 on Moisture Content and Lithology. *Proceedings of the Symposium on Applications of*  
858 *Geophysics to Engineering and Environmental Problems (SAGEEP2001)*,  
859 *Environmental and Engineering Geophysical Society, Denver, CO.*  
860 <https://doi.org/10.4133/1.2922904>.
- 861 West, L. J., Handley, K., Huang, Y., & Pokar, M. (2003). Radar frequency dielectric dispersion  
862 in sandstone: Implications for determination of moisture and clay content. *Water*  
863 *Resources Research*, 39.2. <https://doi.org/10.1029/2001WR000923>.
- 864 Winsauer, W. O., Shearin, H. M., Masson, P. H., & Williams, M. (1952). Resistivity of brine-  
865 saturated sands in relation to pore geometry. *AAPG Bull.*, 36, 253–277.  
866 <https://doi.org/10.1306/3D9343F4-16B1-11D7-8645000102C1865D>.

867 Worthington, P. F. (1993). The uses and abuses of the Archie equations, 1: The formation  
 868 factor-porosity relationship. *Journal of Applied Geophysics.*, 30, 215–228.  
 869 [https://doi.org/10.1016/0926-9851\(93\)90028-W](https://doi.org/10.1016/0926-9851(93)90028-W).

870 Yaramanci, U. (2000). Geoelectric exploration and monitoring in rock salt for the safety  
 871 assessment of underground waste disposal sites. *Journal of Applied Geophysics.*, 44,  
 872 181–196.

873

874

875 **Table 5.** (a) Description of the samples considered for the representation of the VZ profile and  
 876 the simulation of water flow with HYDRUS-1D: depth, description, saturated water content ( $\theta_s$   
 877 ), experimental saturated water content ( $\theta_{sExp.}$ ), hydraulic conductivity ( $K_s$ ),  $\alpha$ , and  $n$ .

Geological Unit	Depth (m)	Sample	Description	$\theta_s$ (cm <sup>3</sup> /cm <sup>3</sup> )	$\theta_{sExp.}$ (cm <sup>3</sup> /cm <sup>3</sup> )	$K_s$ (cm/d)	$\alpha$ cm <sup>-1</sup>	$n$ (/)
1	0.00-0.30	S <sub>A</sub>	Soil	0.4735	0.4864	30.24	0.0242	1.15
	0.31-0.60	S <sub>B</sub>	Soil	0.4661	0.4612	53.57	0.0242	1.16
	0.61-0.90	S <sub>C</sub>	Soil	0.5002	0.4162	47.52	0.0366	1.16
2	0.91-1.30	P <sub>A</sub>	Powdery limestone	0.4511	0.4230	7.31	0.0247	1.17
	1.30-3.50	P <sub>B</sub>	Powdery limestone	0.3659	0.3525	0.455	0.0073	1.25
	3.51-4.10	I <sub>A</sub>	Calcareous sand	0.3918	0.3775	35.22	0.0715	1.20
	4.11-4.60	P <sub>C</sub>	Powdery limestone	0.2969	0.3080	0.143	0.0031	1.22
	4.61-4.90	I <sub>B</sub>	Calcareous sand	0.3698	0.4336	285.49	0.1600	1.23
	4.91-5.20	R <sub>A</sub>	Altered rock	0.2984	0.3400	5000	0.5156	1.36
	5.21-5.50	I <sub>B</sub>	Calcareous sand	0.3698	0.4336	285.49	0.1600	1.23
	5.51-6.60	P <sub>D</sub>	Powdery limestone	0.3527	0.3491	0.185	0.0040	1.22
3	6.61-9.00	R <sub>B</sub>	Massive rock	0.1547	0.1499	1.32	0.0150	1.16
	9.01-11.20	R <sub>D</sub>	Massive rock	0.0949	0.1180	0.402	0.0096	1.17
	11.21-11.40	R <sub>C</sub>	Massive rock	0.0504	0.0491	0.0097	0.0014	1.23
	11.41-14.00	R <sub>D</sub>	Massive rock	0.0949	0.1180	0.402	0.0096	1.17
	14.01-16.00	R <sub>E</sub>	Massive rock	0.1172	0.1333	500	0.1266	1.15

---

16.01-19.00     $R_F$     Massive rock    0.1452    0.1639    500    0.1371    1.19

---

878

879

880

881

882

883 **Table 6** : The ranges of the Archie (a, m and n) and CRIM ( $\alpha$  and  $\epsilon_s$ ) parameters used for the

884 inversion and those commonly reported in the literature for limestone formations.

Model	Parameter	Literature (limestone)	Inversion
Archie	a	$0.2 \leq a \leq 2.3$	$0.1 \leq a \leq 10$
	m	$1.6 \leq m \leq 3$	$1.0 \leq m \leq 10$
	n	$1.5 \leq n \leq 2.5$	n = 2
CRIM	$\alpha$	$-1 \leq \alpha \leq 1$	$-1 \leq \alpha \leq 1$
	$\epsilon_s$	$4 \leq \epsilon_s \leq 11$	$1 \leq \epsilon_s \leq 20$

885

886

887

888

889

890

891

892

893

894

895

896

897

898

899

900  
901  
902  
903  
904  
905  
906  
907  
908  
909  
910  
911  
912  
913  
914  
915  
916  
917  
918  
919  
920  
921

**Table 7.** The Archie's petrophysical parameters obtained in the three layers of the model.

<b>Layer</b>	<b>Depth (m)</b>	<b>a</b>	<b>m</b>	<b>n</b>
1	6.61-9.00	0.80	1.60	2.00
2	9.01-14.00	0.70	1.60	2.00
3	14.01-19.00	0.60	1.47	2.00

922

923

924 **Table 8.** The CRIM's petrophysical parameters obtained in the model layers.

Layer	Depth (m)	$\alpha$	$\epsilon_s$
1	6.61-9.00	0.50	7.99
2	9.01-14.00	0.58	7.97
3	14.01-19.00	0.61	8.00

925

926

Journal Pre-proofs